Tuning superconductivity in Ge:Ga using math xmlns="http://www.w3.org/1998/Math/MathML">msup>mrow>mi>Ga/mi>/mrow>mo>+/mo>/msup>/math> implantation energy

Kasra Sardashti, Tri D. Nguyen, Wendy L. Sarney, Asher C. Leff, Mehdi Hatefipour, Matthieu C. Dartiailh, Joseph Yuan, William Mayer, and Javad Shabani

Phys. Rev. Materials **5**, 064802 — Published 22 June 2021

DOI: 10.1103/PhysRevMaterials.5.064802

Tuning Superconductivity in Ge:Ga Using Ga^+ Implantation Energy

Kasra Sardashti[1], Tri D. Nguyen[1,2], Wendy L. Sarney[3], Asher C. Leff[3], Mehdi Hatefipour[1], Matthieu C. Dartiailh[1], Joseph Yuan[1], William Mayer[1], and Javad Shabani[1*]
[1] *Center for Quantum Phenomena, Department of Physics, New York University, NY 10003, USA*
[2] *Department of Physics, City College of New York, City University of New York, NY 10031, USA*
[3] *CCDC U.S. Army Research Laboratory, Adelphi, MD 20783 USA*
(Dated: June 1, 2021)

High-fluence Ga^+ implantation at medium energies is proven to be an effective tool in forming superconducting thin films in Ge. By changing the post-implantation annealing conditions nano-crystalline to single-crystalline Ge matrices have been produced. Irrespective of crystallinity, such processes have mostly led to supersaturated Ge:Ga films where superconductivity is controlled by the extent of coherent coupling between Ga precipitates. Here, we use Ga^+ implantation energy as means to tailor the spatial distribution and the coupling energy of the Ga precipitates. By systematic structural and magneto-transport studies, we unravel the complex connection between the internal structure of Ge:Ga films and their global superconducting parameters. At the shallowest implantation depth, we observe the strongest coupling leading to a robust superconductivity that sustains parallel magnetic fields as high as 9.95 T; above the conventional Pauli paramagnetic limit and consistent with a quasi-2D geometry. Further measurements at mK temperatures revealed an anomalous upturn in perpendicular critical field $B_\perp$ vs temperature whose curvature and thus origin may be tuned between weakly-coupled superconducting arrays and vortex glass states with quenched disorder. This warrants future investigations into Ge:Ga films for applications where tunable disorder is favorable including test-beds for quantum phase transitions and superinductors in quantum circuits.

I. INTRODUCTION

Group IV semiconductors are favored for integration into hybrid semiconductor-superconductor (Sm-S) quantum circuits due to their high purity and compatibility with the highly scalable complementary metal-oxide-semiconductor (CMOS) technologies[1,2]. Germanium (Ge) is particularly compelling for hybrid S-Sm devices because ultra-clean materials with high hole mobility can be achieved[3]. Realizing superconductivity in Ge is believed to facilitate its integration into superconducting circuits. Similar to silicon (Si)[4–6], superconducting phases of Ge have been demonstrated by incorporating large amounts of gallium (Ga) into its lattice[7,8]. For this purpose, Ge substrates underwent medium-energy (i.e., 100 kev) Ga^+ implantation with fluxes in the order of 10^{16} cm^{-2} ($\sim$ 5–8 at.% Ga), followed by annealing at temperatures near the melting point of Ge ($\sim 938°C$)[7–10]. Such high concentrations of Ga can dope Ge beyond metal-insulator transition limits, narrow the band gap, and induce superconductivity in hyperdoped crystals[11,12]. But since Ga has low solubility in Ge (maximum of $\sim$ 1.1% at about 700 °C), its precipitation within the implanted films may be inevitable[13]. Therefore, beside hyperdoping, coherent Josephson coupling between superconducting Ga precipitates can contribute to the global superconductivity in Ge:Ga films[14,15].

In a quest to isolate the effect of hyperdoping on Ge:Ga superconductivity, the near entirety of the efforts so far have focused on controlling the Ga precipitation at a fixed implantation energy (E_{IMP}) of 100 keV, by using the activation annealing conditions (e.g., temperature, time, heating technique) as the primary tuning parameters[7–10,16,17]. Those studies have successfully produced superconducting Ge:Ga films with nano-, poly-, and single-crystalline Ge matrices. In the single-crystalline phase, one expects Ge hyperdoping to be the predominant superconductivity mechanism since minimal microscopic precipitates were observed. However, even at this limit the dopant activation efficiency of only 31.5% was reported for Ga bearing the question as for the contribution of the remaining 68.5% Ga to the superconductivity[10] . Although many efforts have been focused on nullifying the effect of Ga precipitation in Ge, the distributed nature of its superconductivity controlled by the extent of coherent coupling within and in between Ga clusters provides an interesting platform to tune the superconductivity, particularly for applications where high disorder in a short length scale is favorable[14,15,18].

In this work, we use Ga^+ implantation energy E_{IMP} as a parameter to tune Ga distribution within Ge:Ga thin films. By varying activation annealing temperatures (T_{DA}) at each energy, we show a wide E_{IMP} - T_{DA} processing phase space over which global superconductivity in Ge:Ga can be tuned. Through systematic structural and magneto-transport characterization of our Ge:Ga samples, we demonstrate how the distribution as well as the inter-cluster coupling of Ga precipitates determine the eventual superconducting properties of the films. At the shallowest implantation depth, we observe the strongest coupling leading to a robust superconductivity that sustains parallel magnetic fields above the conventional Pauli paramagnetic limit, consistent with a quasi-2D geometry. Furthermore, pronounced crossing zones in the magnetoresistance curves of the films with low E_{IMP} points to disordered systems that potentially host quantum phase transitions (QPTs)[19,20]. Measurements at mK temperatures showed anomalous upturn in perpendicular critical field (B_c) vs temperature pointing to the presence of quenched disorder and vortex glass states. These signatures warrant future investigations into Ge:Ga films for a rather unconventional range of applications such as superinductors[21], magnetic-field-resistant superconducting resonators[22,23] and phase slip qubits[24,25].

II. EXPERIMENTAL DETAILS

Materials Synthesis. Undoped Ge(100) wafers grown by floating zone method with room-temperature resistivity of 40 $\Omega.cm$ were used. Prior to implantation, Ge native oxide was etched using cyclic immersion in 10% HF solution and DI–H_2O. This was followed by the deposition of 30 nm thick SiO_2 top barriers via plasma-enhanced chemical vapor deposition (PECVD). The oxide barrier helps minimize direct damage to the Ge substrates during the ion implantation process. Ga^+ ion implantation processes (by Kroko Inc.) were carried out at 25 keV, 35 keV, 45 keV, and 80 keV with a fixed ion fluence of 4e16 cm^{-2}. Throughout the implantation substrates were held at room temperature. After implantation dopants were activated using rapid thermal annealing (RTA) under 5 standard liter per minute (SLPM) of N_2 flow and at 300 °C to 800 °C, for 1 min.

Transport Measurements. Electrical properties of the samples were evaluated by measuring the differential resistance (i.e., dV/dI), using lock-in amplifiers, for 5 mm x 5 mm samples in Van der Pauw (VdP) geometry. The AC excitation current for the measurements varied between 1 and 20 μA. Measurements from room temperature ($\sim$ 300 K) down to 1.5 K were performed in a Teslatron PT (Oxford Instruments) cryogen-free refrigerator with maximum magnetic field of 12 T (along z-axis). Measurements below 1.2 K were carried out in a Triton dilution refrigerator (Oxford Instruments) with a 3-axis vector magnet, and maximum z field of 6T. Hall measurements were performed on L-shaped bars. Hall bars were fabricated by UV photolithography followed by reactive ion etching of the mesa using CF_4/O_2 gas mixtures for 2-5 min. The resulting mesa heights varied between 500 nm and 1.2 μm (further details in supplementary information).

Structural and Chemical Characterization. Micro-Raman spectroscopy was performed using a Horiba Xplora μ-Raman system with a 532–nm excitation laser and an objective lens of 1000x magnification. Atomic force microscopy (AFM) was performed in order to determine the surface morphology of the superconducting films in details. A Bruker Dimension Fastscan scanning probe microscopy system was used in tapping mode (ScanAsyst mode). The AFM probes used for the measurements were Bruker FASTSCAN-B, made of silicon nitride with triangular tips of 5–12 nm radius.

Electron Microscopy. The crystal morphology of the structures were examined with with transmission electron microscopy (TEM) in a JEOL ARM200F, equipped with a spherical aberration corrector for probe mode, operated at 200 keV. The composition of each films was studied with energy dispersive X-ray spectroscopy (EDS). The samples were prepared with cross-sectional tripod polishing to 20 μm thickness, followed by shallow angle Ar^+ ion milling with low beam energies (≤ 3 keV), and LN_2 stage cooling in a PIPS II ion mill.

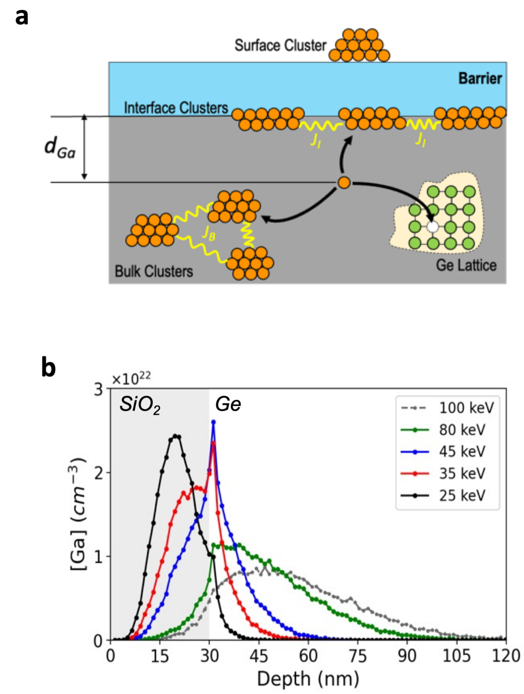

Fig. 1: **a** A schematic detailing the various pathways implanted Ga atoms can take within the Ge matrix, including substituting Ge as a dopant, precipitation within the implanted region, precipitation at the SiO_2/Ge interface, and finally diffusion through the SiO_2 to form Ga surface clusters. The yellow squiggly lines represent the nearest neighbour coupling between the Ga clusters within the bulk (J_B) or at the interface (J_I). **b** One-dimensional simulation of Ga concentration vs depth for various implantation energies from 25 keV to 100 keV, calculated by TRIM for Ga^+ fluence of $4 \times 10^{16}\ cm^{-2}$.

III. RESULTS AND DISCUSSION

Transport properties vs processing conditions. Figure **1**a displays the pathways Ga ions may take within a Ge substrate during the activation annealing. The SiO_2 barrier depicted on top of the Ge substrate is commonly used to prevent surface damage during ion implantation.

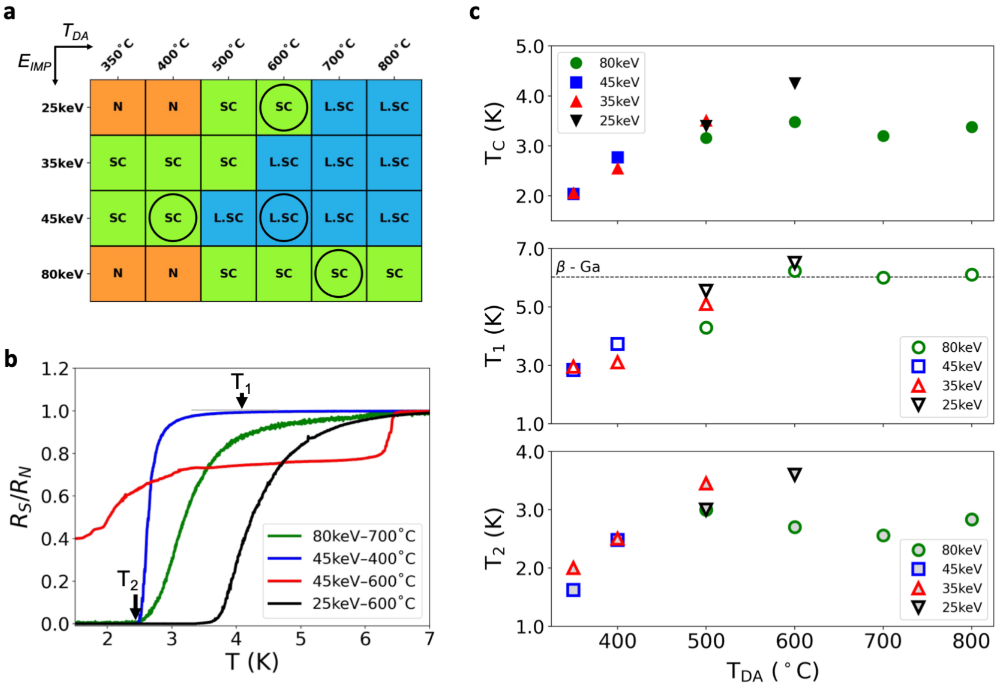

Fig. 2: **a** An overview of transport properties, marked by "N"=normal, "SC"=superconducting, and "L.SC"=locally superconducting, vs processing conditions used in this study i.e. implantation energy E_{IMP} and annealing temperature T_{DA}. **b** Sheet resistance R_S (normalized to sheet resistance at 9K, R_N) vs temperature showing superconducting transitions for four representative processing conditions circled in part **a**. Transition onset and completion temperatures for the blue curve are marked as T_1, and completion T_2, respectively. **c** Superconducting transition midpoint T_c (at $R_S = 0.5R_N$), onset T_1, and completion T_2 vs anneal temperature T_{DA} for samples with complete zero-resistance transitions. The T_c value for β-Ga is adapted from Ref.26.

Due to low solubility, beside occupying Ge sites as a p-type dopant, Ga could precipitate within the implanted region (into bulk clusters) or at the Ge/SiO_2 interface (into interface clusters). At high enough temperatures Ga may even diffuse through the SiO_2 barrier to form surface clusters. The percentage of implanted Ga atoms participating in each process is expected to depend on their depth distribution within the Ge matrix, which in turn is a function of E_{IMP}. Using the Transport of Ions In Matter (TRIM) Monte Carlo software[27], we simulated the Ga depth distribution for E_{IMP} = 25 keV to 100 keV (figure **1**b). The simulation results show that reducing E_{IMP} shifts the Ga distribution peak closer to the top surface enabling stronger Ga confinement near the Ge/SiO_2 interface. This should enable formation of constricted arrays of coupled interface Ga clusters with critical superconducting parameters well beyond that reported for Ge:Ga so far. It should be noted that E_{IMP} = 100 keV is the only value used in previous reports of Ge:Ga superconductivity[8,10,17,28].

Our Ge:Ga films were prepared at E_{IMP} = 25 keV – 80 keV and underwent annealing in a wide temperature range from 300 °C to 800 °C. Figure **2**a shows the E_{IMP}–T_{DA} processing phase space for the Ge:Ga samples prepared in this study. Three groups of samples were identified based on the temperature-dependence of their resistance including: i) superconducting (SC) with transitions to a zero-resistance state; ii) normal (N) with finite resistance and no clear transition down to 1.5 K ; (iii) samples with localized superconductivity (L.SC) as evidenced by a clear drop in resistance at 6–7 K, yet finite resistance at 1.5 K. The difference between the complete and localized superconductivity is highlighted by resistance measurements shown in figure **2**b. Here, four samples are shown that are representative of superconductivity with different Ga depth distributions (see figure S1 for complete resistance measurement data for all processing conditions[29]). The red curve represents a sample with partial superconducting transition at 6.5 K; close to the T_c observed for confined Ga layers in Si[4,6]. This behavior may be ascribed to superconducting Ga clusters that are spaced beyond the length scale necessary for their coherent coupling[15,30]. On the other hand, for samples with complete superconducting transitions, T_c in Ge:Ga does not reach the values for Si:Ga (6–7.5 K), consistent with the presence of proximitized regions with $T_c \approx \Delta exp(-d/\xi_N(T_c))$ following the Lobb, Abraham and Thinkham (LAT) model[31], where Δ is Ga superconducting gap and ξ_N is the normal coherence length in Ge.

A shown in figure **2**b, for superconducting Ge:Ga films, in addition to the conventional critical temperature T_c

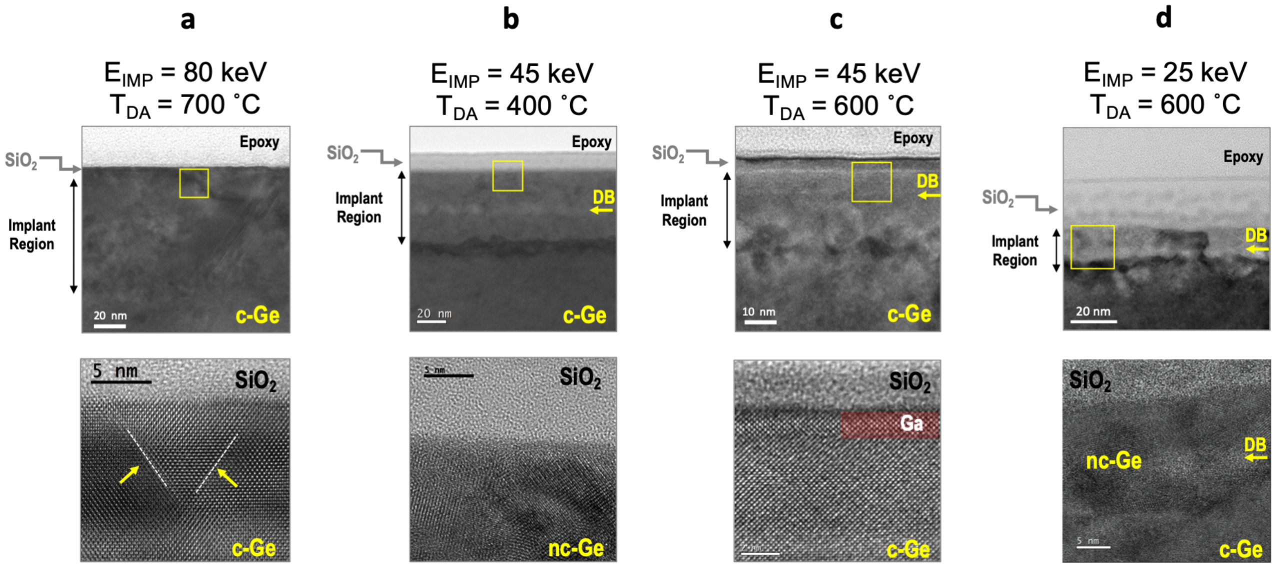

Fig. 3: TEM images of cross-sections prepared on Ge:Ga samples with: **a** E_{IMP} = 80 keV & T_{DA} = 700 °C; **b** E_{IMP} = 45 keV & T_{DA} = 400 °C; **c** E_{IMP} = 45 keV & T_{DA} = 600 °C; **d** E_{IMP} = 25 keV & T_{DA} = 600 °C. The yellow boxes shown in lower magnification images (top row) are visual guides to outline the approximate areas from which the higher magnification images (bottom row) were taken. In section (a), the dotted lines denote stacking faults within the Ge after dopant activation annealing. In (b)–(d), disturbed bands labeled by "DB" are seen as results of SiO_2 recoil during the implantation process.

(at R_S/R_N = 0.5), we follow the temperatures for the onset (T_1) and the completion (T_2) of the transitions. T_1, and T_2 are defined in analogy to the mesoscopic superconductor-metal array model, assuming that Ga clusters separated by heavily-doped p-Ge are the main contributors to the superconductivity[18,32]. According to this model, T_1 represents the phase coherence within the clusters, which depends on their structural state. T_2 shows the extent of inter-cluster coupling (i.e., J_B, J_I) that is dependent on the distance between the clusters and normal coherence length (ξ_N) of the p-Ge channels. Figure **2**c displays plots of T_c, T_1, and T_2 versus T_{DA} at four different implantation energies. When $T_{DA} \geq 600$ °C, T_1 appears to reach an upper limit near the superconducting transition temperature for β–Ga, consistent with the precipitation of phase-coherent β–Ga clusters. At $T_{DA} = 600$ °C, we see superconductivity at both E_{IMP} = 25 keV and 80 keV. Nevertheless, the former E_{IMP}, which results in the shallowest Ga depth profile with Ga clusters in close proximity, has the highest T_2 of 3.6 K; thus a more robust superconducting state is expected at E_{IMP} = 25 keV and T_{DA} = 600 °C. This phase also has a T_c of 4.25 K that is more than 1 K above the record value reported for Ge:Ga[7]. Finally, we note for other energies, including E_{IMP} = 35 keV and 45 keV the annealing window for superconductivity falls below 600 °C. In this regime, wider tunability ranges for T_1 and T_2 are observed as both the crystallinity and spatial distribution of Ga cluster are sensitive to T_{DA}.

To elucidate the role Ga-doping plays in the global superconductivity of the Ge:Ga films, we measured density of holes (n_h) for a pair of samples at each energy E_{IMP} with two different annealing temperatures T_{DA}; one with complete superconducting transition and the other with local or no superconductivity. Details of the Hall measurements are provided in supplementary information (figure S2, table S1[29]). Overall, superconductivity appears over a wide range of hole densities from 3.41 x 10^{15} to 1.07 x 10^{16} cm^{-2}. However, higher n_h does not translate into superconductivity as seen in the pairs of samples with E_{IMP} = 35 keV and 45 keV. In the former, an increase in T_{DA} raised n_h from 5.70 x 10^{15} cm^{-2} to 1.42 x 10^{16} cm^{-2}, but resulted in loss of the superconductivity. In the latter, annealing at higher T_{DA} raised n_h from 5.77 x 10^{15} cm^{-2} to 1.66 x 10^{16} cm^{-2} identically destroying the zero-resistance state above 1.5 K. Therefore, in our processing phase space, we infer superconductivity not to stem from hyperdoping of Ge:Ga effects. Instead, Ga doping affects the inter-cluster coupling, J by changing the conductivity of the Ge matrix surrounding the Ga precipitates. Ga doping of Ge influences hole mobility (μ_h), hole diffusion constant (D), and consequently $\xi_N(T) = \sqrt{\hbar D/k_B T}$. This in turn controls the inter-cluster coupling, which has the standard proximity form of $J_0 exp(-d/\xi_N(T))$ with d being the average inter-cluster spacing[31,33].

Structural and compositional characterization.

To study the influence of E_{IMP} and T_{DA} on Ge:Ga film structures, Transmission Electron Microscopy (TEM) was performed on the four representative samples already identified in figure **2**. The high-resolution TEM images for the samples at low and high magnifications are shown

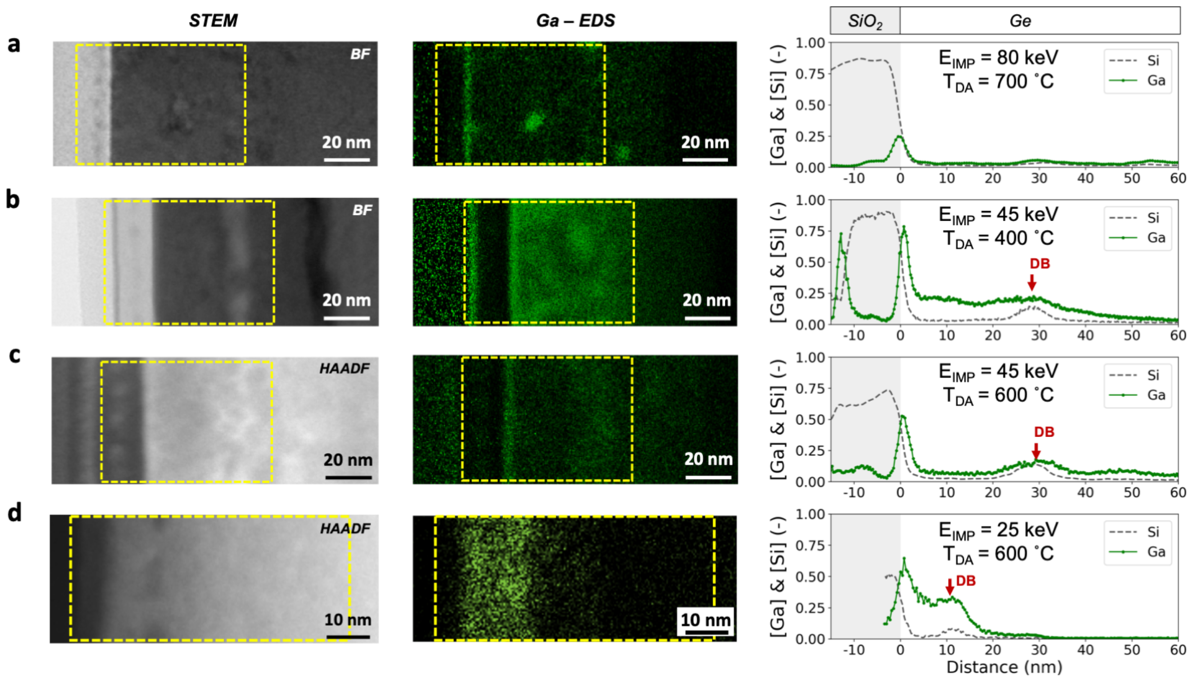

Fig. 4: STEM images and EDS elemental Ga maps for cross-sections of Ga-implanted samples with: **a** E_{IMP} = 80 keV & T_{DA} = 700 °C; **b** E_{IMP} = 45 keV & T_{DA} = 400 °C; **c** E_{IMP} = 45 keV & T_{DA} = 600 °C; **d** E_{IMP} = 25 keV & T_{DA} = 600 °C. The line traces for [Ga] (solid green lines) and [Si] (dotted grey lines), normalized to [Si]+[Ge], are shown on the right. The traces are averaged over the width of the areas outlined by the dotted rectangles in the STEM images and maps. The line traces are aligned by setting the SiO_2/Ge interface to zero distance. Disturbed bands are marked by red arrows and "DB".

in figure **3**. For the film prepared at E_{IMP} = 80 keV & T_{DA} = 700 °C, the implanted region consists of highly crystalline Ge, although with imperfections such as stacking faults (see figure **3**a). Additionally, at certain locations along the SiO_2/Ge interface large crystalline Ga puddles ($\geq$ 25 *nm* wide) were found (not shown here). Dark-field optical microscopy images combined with Raman spectroscopy on identical Ge:Ga films confirmed formation of a poly-crystalline structure with several μm wide grains (see supplementary information figures S3–5[29]).

For Ge:Ga samples with E_{IMP} = 45 keV, shown in figures **3**b and c, the depths of the regions disturbed by the implanting ions appear to be more than 2x smaller. In addition, disturbed bands (DB) $\sim$ 25 nm below SiO_2 caps are present in both samples as a result of Si & O recoil during the implantation. Focusing on the Ge surrounding the disturbed band, annealing at 400 °C forms a nano-crystalline film with a few *nm* wide grains. In contrary, annealing at 600 °C helped recover the crystallinity to a significant level, and allowed formation of a few monolayers thick crystalline Ga at the SiO_2/Ge interface (highlighted in red in figure **3**c). Such crystalline Ga layer appears to be discontinuous as evidenced by its absence in other SiO_2/Ge interface regions. This is consistent with the observation of a transition near 6 K (β-Ga transition[26]) to a non-zero resistance state. The difference in the crystallinity of these two systems was confirmed by electron diffraction measurements (see supplementary figure S6[29]). When E_{IMP} is reduced to 25 keV (see figure **3**d), even after annealing at 600 °C, the Ge:Ga films remain nano-crystalline. And while the depth of the implantation region is reduced to only about 20 nm, a disturbed band is present at approximately 12 nm below the SiO_2/Ge interface. This general trend in the crystallinity of the Ge:Ga films was independently confirmed through via dark-filed optical microscopy and micro-Raman spectroscopy of all the Ge:Ga samples prepared at various E_{IMP} and T_{DA} (see supplementary information figures S3–5[29]).

To better determine the Ga distribution in the samples, the TEM data was complemented by Scanning Transmission Electron Microscopy (STEM) and EDS compositional mapping. Figure **4** shows the STEM images, Ga elemental maps, and line traces for normalized Si & Ga concentrations (i.e. [Ga] = Ga%/ (Si%+Ge%)) in the four samples discussed above. For the sample with E_{IMP} = 80 keV (figure **4**a), the bulk of the implanted region shows [Ga] below 5%, but Ga precipitation is apparent as bulk nano-clusters (diameter $\sim$ 5 nm) and interface clusters near SiO_2/Ge. At E_{IMP} = 45 keV & T_{DA} = 400 °C (figure **4**b), in addition to higher interfacial Ga cluster density, much larger concentrations of Ga ($\geq$ 0.2) are evenly distributed within the implanted region.

When annealed at 600 °C (figure **4**c), Ga atoms diffuse through the structure both toward the Ge substrate and the top barrier as evidenced by reduced [Ga] within the implanted region and enhanced [Ga] below the disturbed band. For the sample with $E_{IMP} = 25$ keV, where implantation has the shallowest depth (figure **4**d), large amounts of Ga ([Ga] ≥ 0.35) are distributed over only a 20 nm wide region, yet with large accumulation at the SiO_2/Ge interface. In this case, the distribution region is too thin for the STEM to resolve individual Ga clusters. Moreover, in elemental maps from all samples with $E_{IMP} \leq$ 45 keV, presence of the disturbed band is confirmed by the peaks in Si, Ga, and O concentration profiles, consistent with the occurrence of SiO_x recoil events for lower Ga^+ implantation energies (for complete sets of elemental profiles see supplementary figure S7[29]). These results confirm that E_{IMP} not only changes the Ga depth distribution, but it determines it precipitation dynamics at various annealing temperatures. It should also be noted that only small concentrations of Ga ([Ga] ≤ 0.15) may be trapped within bulk of SiO_2 capping layers. Trapped [Ga] is slightly higher when $T_{DA} = 400$°C due to insufficient thermal energy available for Ga diffusion through amorphous SiO_2. Nonetheless, for all annealing temperatures broad Ga peaks are present at SiO_2/Ge interfaces. Therefore, the Ga interface clusters may be distributed between the Ge substrate and near-interface region inside the SiO_2 cap. Distribution of Ga clusters in this manner should contribute to the disorder signatures observed in the global superconductivity of the Ge:Ga films.

The locations of the superconducting regions in Ge:Ga films are further revealed by etching the SiO_2 barriers after annealing using 6:1 buffer oxide etchant (BOE). Despite no effect on the microstructure and minimal reactivity with Ga, the etchant is expected to remove Ga through removal of its host matrix (Ge and SiO_2)[34]. Resistance measurements for four superconducting samples before and after BOE etch are shown in figure **5**. Only the Ge:Ga sample with $E_{IMP} = 80$ keV retains its superconductivity after the BOE etch, although with lower T_c and B_c (see supplementary information figure S8 and S9 for further details[29]). This is consistent with a portion of the superconductivity to stem from coherent Josephson coupling between the bulk Ga nano-clusters dispersed deeper within the 80 - 100 nm deep implanted region[30]. In contrast, for samples with $E_{IMP} \leq 45$ keV, the zero-resistance state is destroyed by the BOE etch. At E_{IMP} = 35 keV & 45 keV, some fractions of coupled Ga clusters may still be present deeper in the film as evidenced by the partial resistance dips after the etch. For the sample with $E_{IMP} = 25$ keV however, a fully metallic behavior is observed after the etch consistent with its complete localization of its superconductive phase near the SiO_2/Ge interface.

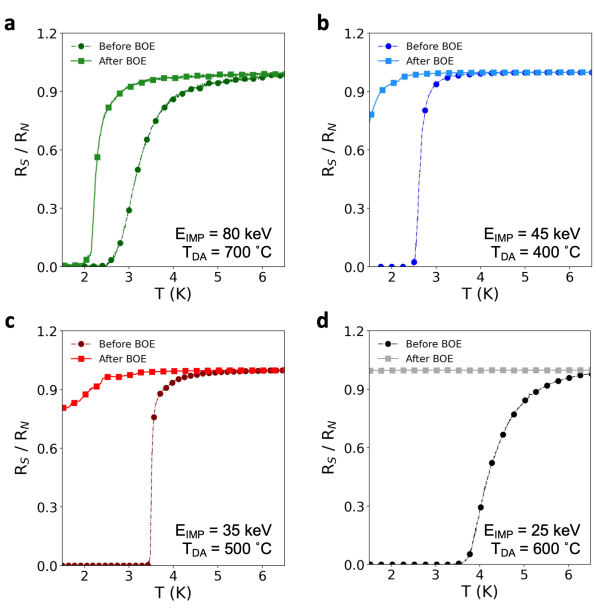

Fig. 5: Normalized resistance vs. temperature for four samples before (dash-dotted line) and after etching the SiO_2 cap (solid line) including: (a)$E_{IMP} = 80$ keV & $T_{DA} = 700$ °C; (b) $E_{IMP} = 45$ keV & $T_{DA} = 400$ °C; (c) $E_{IMP} = 35$ keV & $T_{DA} = 500$ °C; (d) $E_{IMP} = 25$ keV & $T_{DA} = 600$ °C. For the oxide etch, 15 s dip in 6:1 buffer oxide etchant (BOE) was followed by 30 s of DI–H_2O rinse.

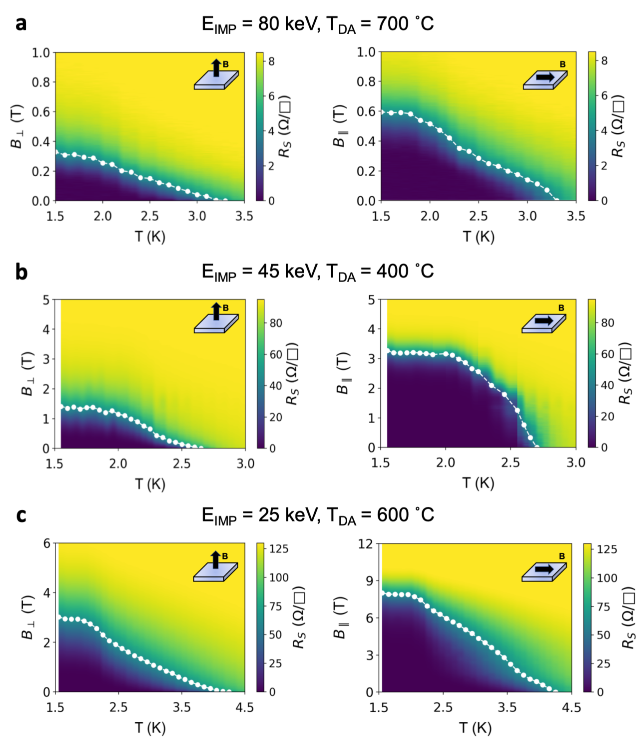

Fig. 6: Sheet resistance maps vs temperature T and magnetic field applied parallel ($B_\perp$) and perpendicular ($B_\parallel$) to the surface of the samples prepared at: **a** $E_{IMP} = 80$ keV & $T_{DA} = 700$ °C; **b** $E_{IMP} = 45$ keV & $T_{DA} = 400$ °C; **c** E_{IMP} = 25 keV & $T_{DA} = 600$ °C. The white overlay plot on each map outlines the normal-superconductor transition boundary, taken at points where $R_s = 0.5\ R_n$.

Temperature dependence of Resistive Critical Fields. Next, we study the temperature dependence of sheet resistance R_S in perpendicular ($B_\perp$) and parallel ($B_\parallel$) magnetic fields as high as 12 T. Figure **6** displays R_s maps vs temperature and magnetic field for the three of the representative Ge:Ga films shown in figure **2**b that exhibit complete superconducting transitions. The resistive critical field (B_c) at each temperature is defined as the field at which $R_s = 0.5\ R_n$. The overlay plots in figure **6** indicate temperature dependence of B_c, which is often known as the boundary for the superconducting-normal phase transition[14,35]. A comprehensive version of B_c(T) phase boundaries for all superconductive Ge:Ga samples is provided in the supplementary information (figure S10[29]).

TABLE I: Summary of superconducting characteristics for three of the Ge:Ga samples prepared in this study. $B_\perp$ and $B_\parallel$ values are measured at 1.55 K. Coherence length at zero temperature, $\xi(0)$ is estimated from the linear Ginzburg-Landau relation near T_c.

E_{IMP} (keV)	T_{DA} (°C)	T_c (K)	$B_\perp$ (T)	$B_\parallel$ (T)	$\xi(0)$ (nm)	l (nm)	$\xi_N(T_2)$ (nm)
80 keV	700	3.3	0.32	0.59	19.7	17	126
45 keV	400	2.65	1.39	3.22	7.0	2.3	47
25 keV	600	4.25	2.97	7.95	6.1	3.3	46

Table I summarizes the key superconducting parameters extracted from the magneto-transport measurements shown in figure **5**a–c. The B_c(T) phase boundaries outlined in figure **5** show significant deviations from the Bardeen-Cooper-Schrieffer (BCS) and Werthamer-HelfandHohenberg (WHH) models. Therefore, instead of reporting zero-temperature critical magnetic fields (B_0), we limit our discussion to $B_\perp$ and $B_\parallel$ at 1.55 K; near the base temperature of our cryostat. Those values are compared to the Pauli paramagnetic limit for the upper critical field, estimated for disordered type-II superconductors as $B_c = 1.8\ T_c$[36,37]. The Ge:Ga film prepared at E_{IMP} = 80 keV has parallel and perpendicular B_c values well below the Pauli limit of 5.94 T. When E_{IMP} is lowered to 45 keV we see significant increases in both the perpendicular and parallel B_c as they near their Pauli limit of 4.77 T. Finally, when E_{IMP} = 25 keV, $B_\parallel$ surpasses the CC limit of 7.65 T by 0.3 T. Similar behavior has been reported for thin lead films, where the large B_c is attributed to strong spin-orbit coupling in the 2D metal[38]. This situation may similarly apply to Ge:Ga films with pseudo-2D superconductivity where ultra-thin Ga clusters are coupled by heavily-doped Ge weak-links.

To further evaluate the quality of our Ge:Ga films as a function of E_{IMP}, we estimated the zero-temperature coherence length, $\xi(0)$. In the vicinity of T_c we observe linear $B_\perp$(T) behavior for the three samples at R(B)= 0.9 R_N. We fit the resulting curves to the linear Ginzburg–Landau relationship $B_\perp = \phi_0/(2\pi\xi(0)^2)(1-T/T_c)$, where ϕ_0 is the flux quantum at zero temperature[39]. Using normal sheet resistance R_N measured at 10 K and carrier concentrations we estimate the mean free path for holes (l). All three samples can be identified as "dirty" superconductors since $\xi(0) > l$; although reducing E_{IMP} makes for a dirtier system ($\xi(0) > 1.5l$) as nano-crystalline Ge matrix becomes the predominant phase post activation annealing. Additionally, by approximating the total thickness of the electrically active region, we determine the bulk hole concentration n. From n we obtained the Fermi velocity $v_F = \hbar/m_h(3\pi^2 n)^{1/3}$ and thus the diffusion constant $D = \frac{1}{3}v_F l$ in the Ge matrix. This leads us to the normal coherence length $\xi_N(T_2) = \sqrt{\hbar D/k_B T_2}$ as presented in Table I. The larger $\xi_N T_2$) of 126 nm at E_{IMP} = 80 keV shows that coupling coupling could occur between Ga clusters at larger distances; this is consistent with the sub-surface superconductive layer observed in this sample. Based on the average Ga cluster distance that could be resolved by electron microscopy ($\leq$ 20 nm), it is rather certain that inter-cluster spacing $d \ll \xi_N(T_2)$ for all samples. This implies the presence of a minimum inter-cluster coupling $J \sim J_0 exp(-d/\xi_N)$ that has to be overcome prior to observing coherent superconductivity across the samples, which may persist even at T=0[18]. The higher T_c and T_2 values for the sample with E_{IMP} = 25 keV confirms that the average d is much smaller ξ_N.

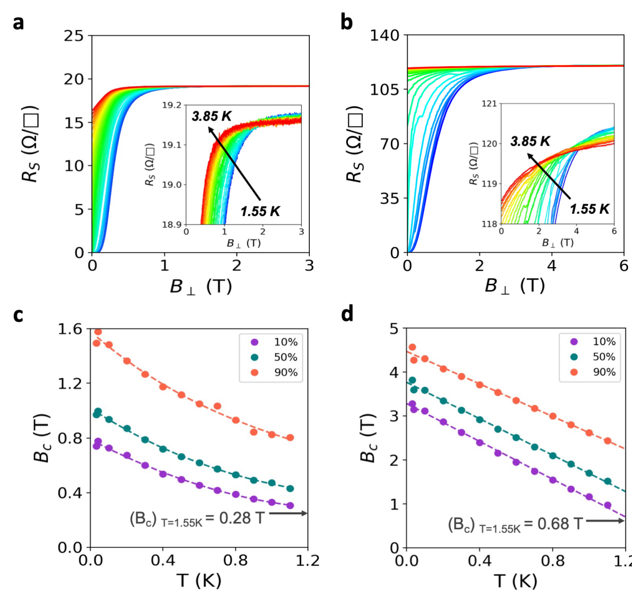

Fig. 7: Magnetoresistance and critical field measurements. R_s as a function of magnetic field for superconducting Ge samples with **a** E_{IMP} = 80 keV & T_{DA} = 700 °C and **b** E_{IMP} = 45 keV & T_{DA} = 400 °C at 1.55 K–3.85 K. B_c vs temperature extracted from R_s(B) measurements at 35 mK – 1.1 K for **c** E_{IMP} = 80 keV & T_{DA} = 700 °C and **d** E_{IMP} = 45 keV & T_{DA} = 400 °C. For all the measurements, the magnetic field is applied perpendicular to the sample surface.

Relatively large critical fields with complex temperature dependence are not the only signatures of disordered superconductivity in the Ge:Ga films with shallow Ga profiles. Figure **7** a & b display the $R_s(B)$ isotherms, measured between 1.55 and 3.85 K, for two samples with E_{IMP} = 80keV & T_{DA} = 700 °C (a) and E_{IMP} = 45keV & T_{DA} = 400 °C (b). In each sample the crossing points in $R_s(B)$ were seen at 1.9 T and 4 T, respectively. This crossing may be an evidence of quantum phase transition (QPT) in quasi-2D disorder superconductors[19,40,41]. R_s (T) behavior vs magnetic field (supplementary figure S11[29]), indicated a more obvious superconductor-metal transition (SMT) from dR/dT<0 to dR/dT>0 for the sample with E_{IMP} = 45 keV. Because of clear SMT along with better-resolved $R_s(B)$ crossings, we conducted scaling analysis on this sample for the possibility of observing Griffiths singularity behavior with divergent product of correlation length exponent (ν) and dynamical critical exponent (z)[42,43]. Details of scaling analysis are provided in the supplementary information (see figure S12[29]). For the sample with E_{IMP} = 45 keV, scaling analysis yielded $z\nu = 2.58 \pm 0.46$ at T = 1.55–1.95 K range, followed by $z\nu = 0.29 \pm 0.01$ at T = 2.15–2.55 K range. Similar analysis on a sample with E_{IMP} = 25 keV led to $z\nu$ of 0.65 ± 0.04 at T = 1.55–1.95 K and 0.4 ± 0.01 at T = 2.15–2.55 K (supplemental figure S13[29]). While these values do not establish a trend toward divergent dynamical critical exponents, the general $z\nu$ behavior warrants further investigation into their SMT at near-zero temperatures and higher magnetic fields.

Another signature of anomaly was observed in Ge:Ga samples when B_c temperature dependence was measured at mK temperatures (i.e. 35 mK – 1.1 K). As shown in figure **7** c & d, both samples with E_{IMP} = 80 keV & T_{DA} = 700 °C (c) and E_{IMP} = 45 keV & T_{DA} = 400 °C (d), show anomalous rise in B_c as temperature approaches 0 K. To evaluate the B_c (T) behavior over a wider temperature range, B_c vs T/T_c curves from 35 mK to T_c for the two samples are provided in the supplementary information (see figure S14[29]). The anomaly persists regardless of the definition used for B_c, including fields at critical sheet resistance of $R_c = 0.1\ R_n$, 0.5 R_n and 0.9 R_n. The B_c vs T upturn is yet another evidence of disorder in these system. The more interesting feature is the difference between the B_c upturn between the two samples; from positive curvature in figure **7**c to linear in figure **7**d. The positive curvature of $B_c(T)$ can be explained by a model of superconducting island weakly coupled via Josephson effect, in which the value of the B_c is determined by an interplay between proximity effect and quantum phase fluctuations[44]. In turn, the linear $B_c(T)$ anomaly has been recently attributed to vortex glass ground states and their thermal fluctuations confined in a disordered 2D geometry[45]. This picture is once again in agreement with the tunability of the global superconducting phase in Ge:Ga through variation of E_{IMP}; sensitivity to quantum fluctuations vs thermal fluctuations may be tailored by the extent of Ga atoms' spatial confinement.

IV. SUMMARY AND CONCLUSION

To summarize, we demonstrated a pathway to tune the superconductivity in Ge:Ga thin films using Ga^+ implantation energy (E_{IMP}) as the main parameter. By systematically monitoring the structural and magneto-transport characteristics of Ge:Ga samples over a wide E_{IMP}-T_{DA} phase space, we determined the conditions to tune the critical superconductivity parameters (i.e., T_c, B_c) to record high values for Ge:Ga thin films. This includes $T_{c,50\%}$ of 4.1 K and parallel B_c of 7.95 T measured for the pseudo-2D Ge:Ga prepared at E_{IMP}=25 keV. At mK temperatures anomalous upturns in $B_c(T)$ were observed for the first time in Ge:Ga films. While the origin of the anomaly is to be determined, we showed that its temperature dependence can be tuned by implantation energy. Further investigations for films with very shallow implantation depths may be necessary to determine the exact nature of this behavior at near-zero temperatures. Furthermore, our results warrants investigations into tunability of disorder in Ge:Ga thin-film systems as test-beds for quantum phase transition studies as well as platforms for superconducting circuits with high kinetic inductance.

1. Y.-P. Shim and C. Tahan, Nat. Commun. **5**, 4225 (2014).
2. Y.-P. Shim and C. Tahan, IEEE J. Sel. Top. Quantum Electron. **21**, 1 (2015).
3. G. Scappucci, C. Kloeffel, F. A. Zwanenburg, D. Loss, M. Myronov, J.-J. Zhang, S. De Franceschi, G. Katsaros, and M. Veldhorst, Nat. Rev. Mater. (2020).
4. R. Skrotzki, J. Fiedler, T. Herrmannsdörfer, V. Heera, M. Voelskow, A. Mücklich, B. Schmidt, W. Skorupa, G. Gobsch, M. Helm, et al., Appl. Phys. Lett. **97**, 192505 (2010).
5. B. Thorgrimsson, T. McJunkin, E. R. MacQuarrie, S. N. Coppersmith, and M. A. Eriksson, J. Appl. Phys. **127**, 215102 (2020).
6. K. Sardashti, T. Nguyen, M. Hatefipour, W. L. Sarney, J. Yuan, W. Mayer, K. Kisslinger, and J. Shabani, Appl. Phys. Lett. **118**, 073102 (2021).
7. J. Fiedler, V. Heera, R. Skrotzki, T. Herrmannsdörfer, M. Voelskow, A. Mücklich, S. Facsko, H. Reuther, M. Perego, K.-H. Heinig, et al., Phys. Rev. B **85**, 134530 (2012).
8. T. Herrmannsdörfer, V. Heera, O. Ignatchik, M. Uhlarz, A. Mücklich, M. Posselt, H. Reuther, B. Schmidt, K.-H. Heinig, W. Skorupa, et al., Phys. Rev. Lett. **102**, 217003 (2009).
9. R. Skrotzki, T. Herrmannsdörfer, V. Heera, J. Fiedler, A. Mücklich, M. Helm, and J. Wosnitza, Low Temp. Phys.

37, 877 (2011).
10. S. Prucnal, V. Heera, R. Hübner, M. Wang, G. P. Mazur, M. J. Grzybowski, X. Qin, Y. Yuan, M. Voelskow, W. Skorupa, et al., Phys. Rev. Mater. **3**, 054802 (2019).
11. M. L. Cohen, Phys. Rev. **134**, A511 (1964).
12. X. Blase, E. Bustarret, C. Chapelier, T. Klein, and C. Marcenat, Nat. Mater. **8**, 375 (2009).
13. R. W. Olesinski and G. J. Abbaschian, Bulletin of Alloy Phase Diagrams **6**, 258 (1985).
14. B. Spivak, P. Oreto, and S. A. Kivelson, Phys. Rev. B **77**, 214523 (2008).
15. S. John and T. C. Lubensky, Phys. Rev. B **34**, 4815 (1986).
16. T. Herrmannsdörfer, R. Skrotzki, V. Heera, O. Ignatchik, M. Uhlarz, A. Mücklich, M. Posselt, B. Schmidt, K.-H. Heinig, W. Skorupa, et al., Supercond. Sci. Technol. **23**, 034007 (2010).
17. V. Heera, J. Fiedler, M. Naumann, R. Skrotzki, S. Kölling, L. Wilde, T. Herrmannsdörfer, W. Skorupa, J. Wosnitza, and M. Helm, Supercond. Sci. Technol. **27**, 055025 (2014).
18. S. Eley, S. Gopalakrishnan, P. M. Goldbart, and N. Mason, Nat. Phys. **8**, 59 (2012).
19. Y. Xing, H.-M. Zhang, H.-L. Fu, H. Liu, Y. Sun, J.-P. Peng, F. Wang, X. Lin, X.-C. Ma, Q.-K. Xue, et al., Science **350**, 542 (2015).
20. Y. Saito, T. Nojima, and Y. Iwasa, Nat. Commun. **9**, 778 (2018).
21. T. Hazard, A. Gyenis, A. Di Paolo, A. Asfaw, S. Lyon, A. Blais, and A. Houck, Phys. Rev. Lett. **122**, 010504 (2019).
22. D. Niepce, J. Burnett, and J. Bylander, Phys. Rev. Appl. **11**, 044014 (2019).
23. N. Samkharadze, A. Bruno, P. Scarlino, G. Zheng, D. DiVincenzo, L. DiCarlo, and L. Vandersypen, Phys. Rev. Appl. **5**, 044004 (2016).
24. J. T. Peltonen, P. C. J. J. Coumou, Z. H. Peng, T. M. Klapwijk, J. S. Tsai, and O. V. Astafiev, Sci. Rep. **8**, 10033 (2018).
25. O. V. Astafiev, L. B. Ioffe, S. Kafanov, Y. A. Pashkin, K. Y. Arutyunov, D. Shahar, O. Cohen, and J. S. Tsai, Nature **484**, 355 (2012).
26. D. Campanini, Z. Diao, and A. Rydh, Phys. Rev. B **97**, 184517 (2018).
27. J. F. Ziegler, *The Stopping and Ranges of Ions in Matter: Handbook of Stopping Cross-Sections for Energetic Ions in All Elements* (Elsevier, 2013).
28. J. Fiedler, V. Heera, R. Skrotzki, T. Herrmannsdörfer, M. Voelskow, A. Mücklich, S. Oswald, B. Schmidt, W. Skorupa, G. Gobsch, et al., Phys. Rev. B **83**, 214504 (2011).
29. *See Supplemental Material at [URL will be inserted by publisher] for additional details on resistivity measurements, Hall measurements, structural characterization of the Ge:Ga films, temperature dependence of critical magnetic field in all superconducting Ge:Ga samples, as well as finite-size caling analysis.*
30. G. Deutscher, I. Grave, and S. Alexander, Phys. Rev. Lett. **48**, 1497 (1982).
31. C. J. Lobb, D. W. Abraham, and M. Tinkham, Phys. Rev. B **27**, 150 (1983).
32. S. Eley, S. Gopalakrishnan, P. M. Goldbart, and N. Mason, J. Phys.: Condens. Matter **25**, 445701 (2013).
33. D. W. Abraham, C. J. Lobb, M. Tinkham, and T. M. Klapwijk, Phys. Rev. B **26**, 5268 (1982).
34. W. C. Johnson, J. B. Parson, and M. C. Crew, J. Phys. Chem. **36**, 2651 (1932).
35. M. P. A. Fisher, Phys. Rev. B **36**, 1917 (1987).
36. A. M. Clogston, Phys. Rev. Lett. **9**, 266 (1962).
37. B. S. Chandrasekhar, Appl. Phys. Lett. **1**, 7 (1962).
38. H. Nam, H. Chen, T. Liu, J. Kim, C. Zhang, J. Yong, T. R. Lemberger, P. A. Kratz, J. R. Kirtley, K. Moler, et al., Proc. Natl. Acad. Sci. U.S.A. **113**, 10513 (2016).
39. A. W. Tsen, B. Hunt, Y. D. Kim, Z. J. Yuan, S. Jia, R. J. Cava, J. Hone, P. Kim, C. R. Dean, and A. N. Pasupathy, Nat. Phys. **12**, 208 (2016).
40. Y. Liu, Z. Wang, P. Shan, Y. Tang, C. Liu, C. Chen, Y. Xing, Q. Wang, H. Liu, X. Lin, et al., Nat. Commun. **10**, 3633 (2019).
41. C. Zhang, Y. Fan, Q. Chen, T. Wang, X. Liu, Q. Li, Y. Yin, and X. Li, NPG Asia Mater. **11**, 1 (2019).
42. N. Marković, C. Christiansen, and A. M. Goldman, Phys. Rev. Lett. **81**, 5217 (1998).
43. M. P. A. Fisher, P. B. Weichman, G. Grinstein, and D. S. Fisher, Phys. Rev. B **40**, 546 (1989).
44. V. M. Galitski and A. I. Larkin, Phys. Rev. Lett. **87**, 087001 (2001).
45. B. Sacépé, J. Seidemann, F. Gay, K. Davenport, A. Rogachev, M. Ovadia, K. Michaeli, and M. V. Feigelman, Nat. Phys. **15**, 48 (2019).

Data Availability.

The data that support the findings of this study are available within the paper and its supplementary Information. Additional data are available from the corresponding author upon request.

Acknowledgements

The authors thank Emanuel Tutuc and Fatemeh Barati for fruitful discussions. NYU team is supported by AFOSR Grant No. FA9550-16-1-0348 and ARO Grant No. W911NF1810115. K.S. thanks Davood Shahjerdi and Edoardo Cuniberto for their assistance with the Raman spectroscopy measurements. J.Y. acknowledges funding from the ARO/LPS QuaCGR fellowship reference W911NF1810067.